

# STARE AND CHASE: OPTICAL POINTING DETERMINATION, ORBIT CALCULATION AND SATELLITE LASER RANGING WITHIN A SINGLE PASS

Michael A. Steindorfer<sup>(1)</sup>, Georg Kirchner<sup>(1)</sup>, Franz Koidl<sup>(1)</sup>, Peiyuan Wang<sup>(1)</sup>, Alfredo Antón<sup>(2)</sup>, Jaime Fernández<sup>(2)</sup>, Diego Escobar<sup>(2)</sup>, Jiri Silha<sup>(3)</sup>, Klaus Merz<sup>(4)</sup>

<sup>(1)</sup> Space Research Institute, Austrian Academy of Sciences, Lustbuehelstrasse 46, 8042 Graz, Austria  
Email: [michael.steindorfer@oeaw.ac.at](mailto:michael.steindorfer@oeaw.ac.at), [georg.kirchner@oeaw.ac.at](mailto:georg.kirchner@oeaw.ac.at), [franz.koidl@oeaw.ac.at](mailto:franz.koidl@oeaw.ac.at),  
[peiyuan.wang@oeaw.ac.at](mailto:peiyuan.wang@oeaw.ac.at)

<sup>(2)</sup> GMV Aerospace and Defence, Calle Isaac Newton 11, 28760 Tres Cantos, Spain  
Email: [amanton@gmv.com](mailto:amanton@gmv.com), [jfernandez@gmv.com](mailto:jfernandez@gmv.com), [descobar@gmv.com](mailto:descobar@gmv.com)

<sup>(3)</sup> Astronomical Institute University of Bern, Sidlerstrasse 5, 3012 Bern, Switzerland  
Email: [jiri.silha@aiub.unibe.ch](mailto:jiri.silha@aiub.unibe.ch)

<sup>(4)</sup> Space Debris Office, ESA/ESOC, Robert Bosch Strasse 5, 64293 Darmstadt, Germany  
Email: [klaus.merz@esa.int](mailto:klaus.merz@esa.int)

## ABSTRACT

The increasing amount of space debris in orbit around Earth poses a serious threat to active satellites or space stations. A profound knowledge of the orbit of space debris is necessary for both collision avoidance and future removal approaches. The presented Stare and Chase concept combines a survey sensor and a tracking sensor with each other. An extensive simulation campaign is performed to analyse orbit determination algorithms in dependence of various orbital parameters. Within an experimental campaign an astronomical camera with a wide field of view was used to derive pointing information to uncooperative targets. After initial orbit determination using the derived pointing angles satellite laser ranging was achieved within the same pass without a-priori orbit information.

Keywords: Space Debris, Plate Solving, Satellite Laser Ranging, Space Surveillance and Tracking, Initial Orbit Determination

## 1 INTRODUCTION

The increasing number of space debris around Earth poses a great threat to active satellites in space [1]. In addition to approx. 1000 active and 1000 inactive satellites by applying scientific models [2] and radar measurements it was estimated that approx. 30000 objects larger than 10 cm and more than 700000 objects larger than 1 cm are in orbit around Earth [3,4]. An impact even of small particles on an active satellite with an orbital velocity of approx. 7 km/s can lead to serious damage [5].

Any improvement of re-entry predictions as well as approaches to active debris removal need not only profound knowledge of the orbit but also of the attitude (spin parameters) which can be obtained via laser ranging [6-9].

Tracking space debris objects using a priori information (e.g. from an existing catalogue) allows to cover significant fractions of the orbital period producing accurate orbit determinations which results in a good knowledge of the orbital parameters of the object. However, a more complete characterisation of the near-Earth environment is necessary; including non-catalogued debris (e.g. resulting from fragmentations) as well. Surveillance sensors are devoted to perform this task, using fixed or predefined pointing laws which are not adapted to the motion of the object, leading to short observation arcs and poor orbital information. There are several examples of these scenarios, such as fence array radars [10], survey telescopes or beam-park experiment [11,12].

*Stare and Chase* is a combination of both scenarios, survey and tracking, allowing to detect new objects and to obtain a good orbital determination simultaneously. This scenario uses multiple sensors which are not necessarily located at the same site but working in close collaboration. Sensors in the “**Stare**” mode, detect all objects crossing through their FOVs while sensors in “**Chase**” mode are ready for an immediate tracking of the detected objects. Stare observations are processed as soon as they are collected to obtain orbit predictions of the object for the tracking sensors as fast as possible. This scenario could also be achieved using only one sensor, changing from stare to chase mode, however two or more sensors are preferred due to their different observation capabilities, accuracy, sensibility or slew agility.

An analysis of the different algorithms to compute the orbit predictions and an extensive set of simulations are presented as preparation for the experimental part: A proof of concept of the stare and chase scenario using a LEO surveillance telescope and Satellite Laser Ranging (SLR). SLR is an excellent method to further improve

orbit predictions up to the order of a few meters [13].

During the framework of this experimental campaign an analogue astronomical camera with a field of view of approx.  $7^\circ$  was used as a surveillance sensor to determine pointing angles to sunlit space debris targets. Within the same pass of the satellite, the orbit calculation results were used to successfully perform space debris laser ranging [14-16] to several targets. A detailed analysis shows the Observed-Minus-Calculated residuals and offsets to TLE predictions.

## 2 INITIAL ORBIT DETERMINATION ALGORITHMS

The algorithms to be implemented for *Stare & Chase* will use observations with two main characteristics: short tracklets (around seconds in case of LEO orbits, some minutes for the higher regime) and a small number of observations (two or three) particularly for telescopes. Additionally, the algorithms shall be fast enough to process the observations and to obtain the orbit predictions within seconds in order to command the tracking without delay. The selected algorithms have been classified regarding two criteria: 1) the number of Keplerian elements that can be estimated and 2) the kind of observations used. The implemented algorithms are summarised on the following sections.

### 2.1 Four Keplerian elements.

#### 2.1.1 One angular and angular rate observation

This algorithm has been extracted from [17]. The geocentric position and velocity of the debris  $\mathbf{r}$  and  $\mathbf{v}$ , can be decomposed as

$$\mathbf{r} = \mathbf{r}_S + \boldsymbol{\rho} = \mathbf{r}_S + \rho \cdot \mathbf{p} \quad (1)$$

And the velocity

$$\mathbf{v} = \mathbf{v}_S + \dot{\rho} \cdot \mathbf{p} + \rho \cdot \boldsymbol{\omega} \wedge \mathbf{p} \quad (2)$$

where  $\mathbf{r}_S$  and  $\mathbf{v}_S$  are the position and the velocity of the sensor,  $\mathbf{p}$  is the pointing vector from the sensor to the debris,  $\rho$  and  $\dot{\rho}$  are the slant range and the range rate respectively and  $\boldsymbol{\omega}$  the angular velocity of the debris with respect to the sensor.

Using a circular orbit hypothesis ( $\mathbf{r} \cdot \mathbf{v} = 0$ ), the equations of Keplerian motion allows to solve a non-linear equation system numerically to compute  $\rho$  and  $\dot{\rho}$ .

#### 2.1.2 Two angular observations

The following algorithm has been extracted from [18]. The radius vectors  $\mathbf{r}_i$  from the centre of the attracting body are

$$\mathbf{r}_i = \mathbf{r}_{Si} + \rho_i \mathbf{p}_i \quad (3)$$

where  $\mathbf{r}_{Si}$  is the position of the sensor,  $\rho_i$  the slant range

and  $\mathbf{p}_i$  the pointing vector from the observer. Assuming a circular orbit the following geometrical solution for  $\rho_i$  could be derived

$$\rho_i = -\mathbf{r}_i \cdot \mathbf{p}_i + \sqrt{(\mathbf{r}_{Si} \cdot \mathbf{p}_i)^2 - (r_{Si}^2 - a^2)} \quad (4)$$

From the dynamical point of view, the Keplerian motion applied to the angular difference  $\Delta\alpha$  between the two observations vectors  $\mathbf{r}_i$  results as:

$$\Delta\alpha = \sqrt{\frac{\mu}{a^3}} (t_2 - t_1) \quad (5)$$

where  $\mu$  is the gravitational parameter,  $a$  the semi-major axis and  $t$  the time of each observation. Using again the hypothesis of a circular orbit, the non-linear equation can be solved for the semi-major axis  $a$ .

#### 2.1.3 One angular, range and range rate observation

This algorithm is also known as Doppler-Inclination method. The first step is the computation of the semi-major axis which can be deduced from the cosine theorem, assuming spherical earth:

$$a^2 = (r_S + h)^2 = r_S^2 + \rho^2 + 2r_S \cdot \rho \cdot \sin \varepsilon \quad (6)$$

where  $h$  is the geocentric altitude of the orbit and  $\varepsilon$  is the topocentric elevation from the observer station.

The velocity can be split into components perpendicular ( $\mathbf{v}_\perp$ ) and parallel ( $\mathbf{v}_\parallel$ ) to the plane defined by position and pointing vectors.

Considering a circular orbit.

$$\mathbf{v}_\parallel \cdot \mathbf{r} = 0 \quad (7)$$

$$\mathbf{v}_\perp \cdot \mathbf{r} = 0 \quad (8)$$

the range rate is defined as:

$$\dot{\rho} = (\mathbf{v} - \mathbf{v}_S) \cdot \frac{\boldsymbol{\rho}}{|\boldsymbol{\rho}|} \quad (9)$$

The projection of the perpendicular component of both object and station velocities onto the pointing vector is zero.

$$\mathbf{v}_\perp \cdot \boldsymbol{\rho} = 0 \quad (10)$$

$$\mathbf{v}_{S\perp} \cdot \boldsymbol{\rho} = 0 \quad (11)$$

Then, range rate can be expressed as:

$$\mathbf{v}_\parallel \cdot \frac{\boldsymbol{\rho}}{|\boldsymbol{\rho}|} - \mathbf{v}_{S\parallel} \cdot \frac{\boldsymbol{\rho}}{|\boldsymbol{\rho}|} = \dot{\rho} \quad (12)$$

As mentioned before,  $\mathbf{v}_\parallel$  can be defined as a linear composition of  $\mathbf{r}$  and  $\boldsymbol{\rho}$ :

$$\mathbf{v}_\parallel = \lambda \mathbf{r} + \mu \boldsymbol{\rho} \quad (13)$$

Finally, using the range rate equation and the projection of  $\mathbf{v}_\parallel$  into a position vector, a linear system is obtained

where  $\lambda$  and  $\mu$  can be solved.

$$\lambda r^2 + \mu(\mathbf{r} \cdot \boldsymbol{\rho}) = 0 \quad (14)$$

$$\lambda(\mathbf{r} \cdot \boldsymbol{\rho}) + \mu \rho^2 = \rho \dot{\rho} + \mathbf{v}_{S\parallel} \cdot \boldsymbol{\rho} \quad (15)$$

Once  $\mathbf{v}_{\parallel}$  is computed, the modulus of  $\mathbf{v}$  is also known using the hypothesis of circular orbit, and then  $\mathbf{v}_{\perp}$  can be finally computed.

## 2.2 Six Keplerian elements.

### 2.2.1 Three angular observations

Computing the orbit from three angular observations is a classical problem of initial orbit determination, which has been widely studied in astronomy since the 18<sup>th</sup> century. The classical algorithms are Laplace, Gauss and Double r-iteration which can be found in [19]. A modern computational approach, including a least squares method, is proposed by Gooding and revisited by Vallado [20,21].

### 2.2.2 Two angular and range observations

This problem represents the classical Lambert's Problem where classical algorithms (minimum-energy, Gauss...) have been collected e.g. by Vallado [19]. Moreover a new approach is presented by Izzo in [22].

### 2.2.3 Three angular and range observations

Two methods are well known in literature to solve this problem: Gibbs and Herrick-Gibbs, both detailed in Vallado [19]. These methods are complementary, Gibbs solution fails when vectors are closely spaced, and Herrick-Gibbs obtains the best results when vectors are close together.

## 3 SIMULATION CAMPAIGN RESULTS

A parametric analysis is executed in order to evaluate the performances and limits of the algorithms for each of the different scenarios proposed in Tab. 3-1:

Table 3-1: Summary of scenarios

	Orbit	Radar	Optical
LEO	500 km	LEO_L_1R	LEO_L_O
	1000 km	LEO_M_1R	LEO_M_O
	1500 km	LEO_H_1R	LEO_H_O
	MEO		MEO_O
	GEO		GEO_O
	HEO	HEO_1R (Perigee)	HEO_O (Apogee)

- Two kinds of measurements, ideal and Gaussian noise, are considered.
- A parametric study is performed in order to evaluate the pointing performance depending on the geometry of the pass and the direction the stare camera points to (Stare point: Azimuth, Elevation).

Observations are simulated at the nominal rate for each sensor during the interval the objects remain in the

FOV. In order to reduce the obtained tracklet to the number of observations required by each algorithm a fitting process is performed using a constant angular acceleration kinematical model (algorithms directly using more measurements were out of the scope of the study).



Figure 3-1: Geometric configuration for LEO scenarios, orbit inclination and traces for different pass geometries.

## 3.1 Radar Scenarios

The algorithms used in this section are:

- Propagation, angular extrapolation of the stare pointing.
- One angular, range and range rate, Doppler Inclination method.
- Two angular and range, Izzo's Lambert method.
- Three angular and range or Gibbs / Herrick-Gibbs methods.

### 3.1.1 LEO

The following contour plots correspond to a zenithal pass – a pass ranging from azimuth 0° to azimuth 180°, reaching at maximum 90° elevation. In some of the following figures passes with lower maximum elevation are considered as well. Stare point direction [%] is defined to make passes with different maximum elevations comparable: 50% means that the sensor points into the direction where exactly one half of the maximum elevation of the pass is reached.

As shown in Figure 3-2, two and three observation algorithms return the best results in terms of accuracy, with a slight advantage of the latter one. Concerning the pass geometry a high pointing error zone appears close to 50° elevation and 10° azimuth.

This effect can be explained considering that for low and high elevation values the range component contains important information necessary for the estimation of the velocity. The same is true for large azimuth values. Hence, at medium elevations / low azimuth the pointing error increases as the algorithms do not obtain enough information from the observations to produce an accurate prediction.

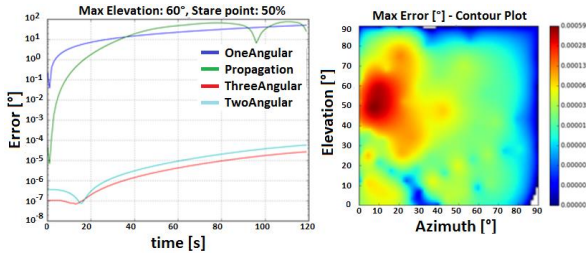


Figure 3-2: Left: Temporal pointing error evolution after stare for different algorithms. Right: Maximum pointing error depending on the stare point position (azimuth/elevation) for the two angular and range method considering a zenithal pass.

Concerning pass geometry, no noticeable differences between different geometries, maximum pass elevation or orbit inclinations can be found (Fig. 3-3). A slight improvement regarding the accuracy is observed for high stare elevations for each pass.

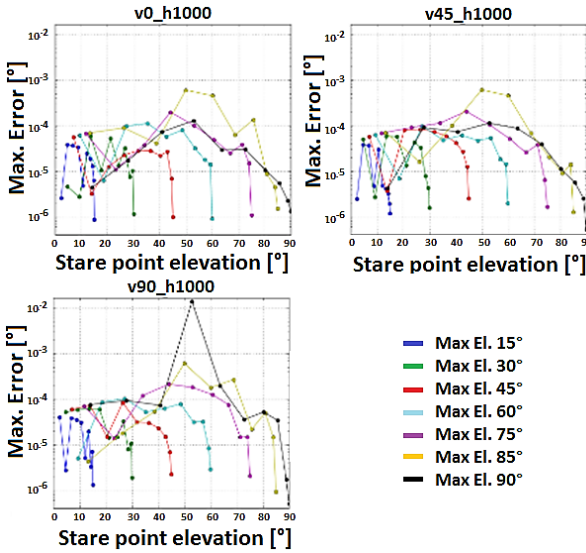


Figure 3-3: Maximum pointing error depending on the stare point elevation and the maximum elevation point for three different orbit inclinations (0°, 45°, 90°).

Regarding the observation noise analysis, an increase of noise level has no direct effect on the accuracy of the orbit due to the way the observations are fitted reducing the tracklet to the number of observations suitable for the algorithm. On the other hand, the size of the field of view has a direct impact on the accuracy of the resulting pointing, larger fields provide longer tracklets, and then more accurate predictions can be computed. However, it is limited by the model used on the fitting and how precise it fits the shape of the tracklet.

### 3.1.2 HEO

Fig 3-4, on the left, shows a comparison for the algorithms allowing to compute non-circular orbits. As it could be expected, the three angular and range method

(Herrick-Gibbs) produces slightly better accuracy results than the two angular and range method (Izzo's Lambert) due to the use of an additional observation.

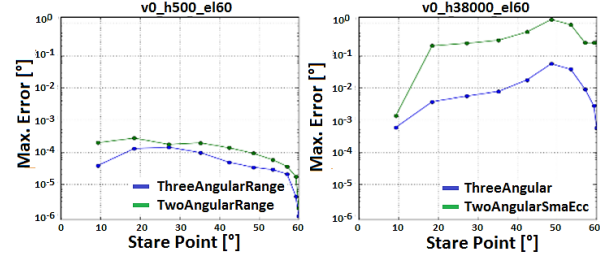


Figure 3-4: Left: Maximum pointing error for a HEO orbit of 500 km perigee using angular and range algorithms. Right: Maximum pointing error for a HEO orbit of 38000 km apogee using angles-only algorithms.

## 3.2 Optical Scenarios

The algorithms used in this section are:

- Propagation, angular extrapolation of the stare pointing.
- One angular and angular rate observation.
- Two angular observations.
- Three angular observations, Gauss method.

### 3.2.1 LEO

The same way as in the previous section, the more observations are used by the algorithms, the better results in terms of accuracy are obtained (Figure 3-5 left). Pointing propagation based on angular fitting produces good results during the stare period, but degrades quickly on extrapolation. Regarding pass geometry, it can be observed (Figure 3-5 on the right) that the worst results are obtained for low elevations and azimuth stare points. Following the same explanation as in the previous section, this behaviour is related to the lack of information obtained from angular observations when the relative motion of the object with respect to the observer is close to the line of sight.

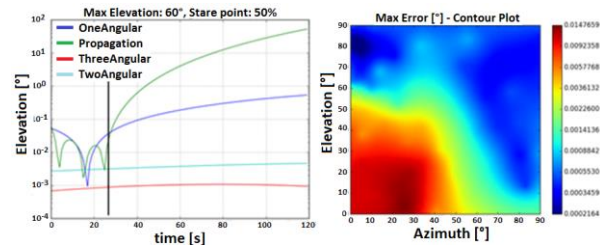


Figure 3-5: Left: temporal pointing error evolution after stare for different algorithms, vertical line means end of stare period. Right, maximum pointing errors depending on the stare point position considering a zenithal pass (Azimuth: 0-180°, Elevation: 0-90°).

The orbit inclination does not affect the accuracy of the prediction (Figure 3-6), however the higher the orbit

altitude the better accuracy is obtained. This is mainly related to the previous explanation about the object relative motion.

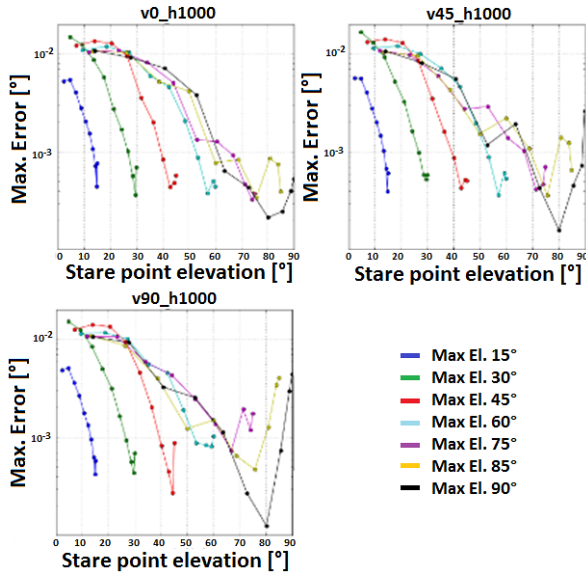


Figure 3-6: Maximum pointing error depending on the stare point elevation and the maximum elevation point for three different orbit inclinations (0°, 45°, 90°).

Finally, an analysis using two different levels of Gaussian noise (0.3 mdeg and 0.6 mdeg) is performed in addition to the ideal observations (Figure 3-7). Measurement noise degrades the pointing accuracy of the predicted pointing, as expected, however, due to the fitting performed on the observations the increase of the noise level has only a small effect.

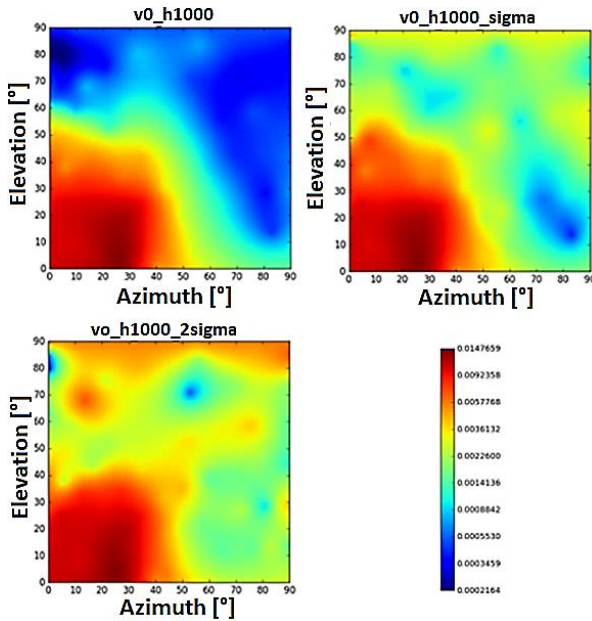


Figure 3-7: Maximum pointing errors depending on the stare point position for three values of Gaussian noise.

### 3.2.2 MEO and GEO

As mentioned previously, for higher orbits angular observations provide more useful information than for lower ones. Consequently, a clear improvement on the accuracy of the orbit is achieved.

Two simulated scenarios are considered: circular orbits at MEO and GEO regimes. The two angular observation algorithms show improved accuracy due to the fact that the eccentricity is not estimated.

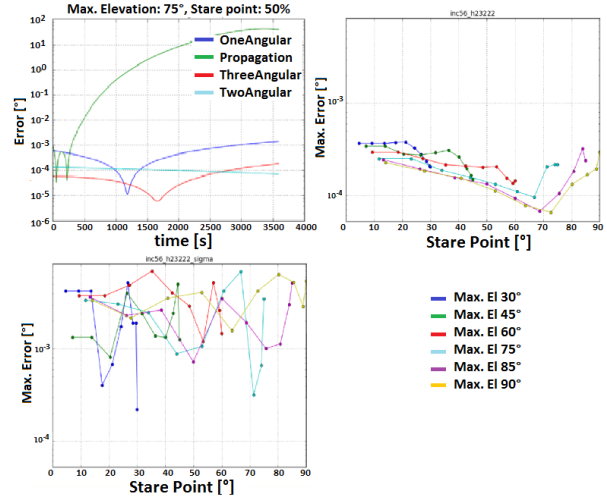


Figure 3-8: Upper-Left: Pointing error evolution from stare. Upper-Right: Maximum pointing errors for ideal observations. Lower-Left: Maximum pointing errors for Gaussian noised observations.

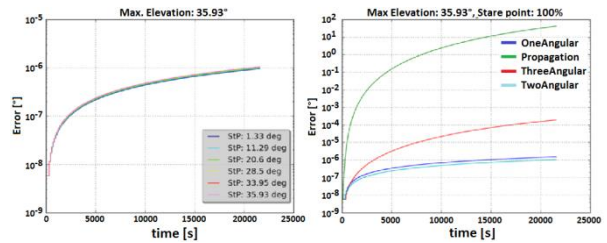


Figure 3-9: Left: Pointing error evolution for different stare elevations. Right: Pointing error evolution for different angles-only algorithms.

## 4 PRELIMINARY OBSERVATION CAMPAIGN

In addition to the previous simulation campaign a preliminary observation campaign is designed in order to check the feasibility of the concept of the scenario using a LEO telescope as stare sensor and an SLR as chase sensor detailed on the following sections.

Figure 4-1 and Figure 4-2 show the results for two satellites equipped with laser retroreflectors, TOPEX and ENVISAT, in order to perform a proof of concept. The pointing prediction is correctly computed by all of the angles-only algorithms which were implemented:

The two angular algorithm presented on the previous section and the Gauss algorithm for three angular observations. The two angular algorithm produces more accurate results thanks to the additional hypothesis of a circular orbit, which is correct for the analysed satellites. On the other hand, the three angles algorithm is not able to estimate the eccentricity of the orbit correctly due to the very short duration of the first tracklet. In both cases, the pointing accuracy is not accurate enough to point directly to the target with SLR, but it is to initialise the SLR search routine.

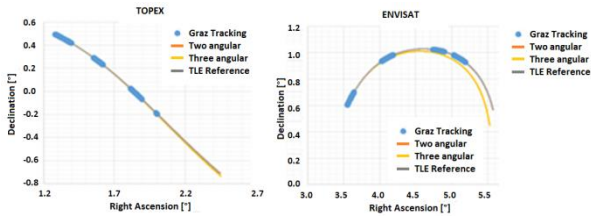


Figure 4-1: Results for two of the algorithms, using two and three angular observations based only on the first tracklet and the comparison with the subsequent tracklets on the same pass and the comparison using TLE.

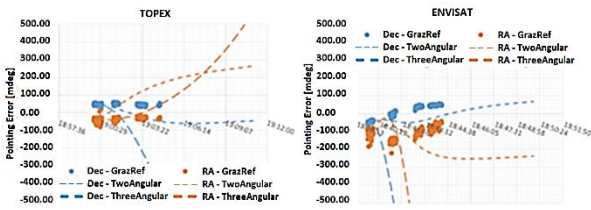


Figure 4-2: Results for two of the algorithms, using two and three angular observations based on the first tracklet and the comparison of the pointing errors with respect the predicted TLE orbit.

## 5 OPTICAL POINTING DETERMINATION

### 5.1 Camera setup

A Watec 910 HX/RC [23] astronomical video camera was equipped with an F/1.4,  $f = 50$  mm photo objective resulting in a field of view of  $7.3 \times 5.5^\circ$ . The camera system was piggyback mounted on top of the satellite laser ranging (SLR) receiving telescope of Graz SLR station and roughly aligned to the optical axis. The camera outputs an analogue video signal via BNC cable which is digitalized by using a video capturing device. A frame rate of 25 / second with a shutter speed of 20 ms allows quasi-real-time monitoring of the night sky. So far the optical observations mostly made use of the analysis of faint streaks in images [24-26].

### 5.2 Plate solving and target recognition

An arbitrary direction of the sky is recorded with the camera system and displays stars up to stellar magnitude

9. Depending on elevation and atmospheric conditions between 50 and 200 stars are visible. The image is converted to black and white and the X/Y coordinates of the stars on the image sensor are monitored. Every two seconds by using a plate solving algorithm [27] the central position (in equatorial coordinates: declination, right ascension of epoch J2000) of the image is determined with an accuracy of approx. 15-20 arc seconds. The approximate initial starting coordinates (within  $1^\circ$ ) are derived from the current altitude / azimuth position of the SLR telescope. The duration of a single plate solve can be reduced to 200-500 ms by using only the 50 brightest stars to perform the analysis.

If a sunlit target passes through the field of view (Fig. 5-1) of the camera it is automatically detected using a self-written algorithm: The current position of all “particles” on the image is compared to its position on a previous frame (e.g. 4 frames earlier). All particles which are “non-moving” are regarded as stars, particles which have moved more than e.g. 15 pixels are regarded as noise and particles which have moved between 2-15 pixels are identified as a satellite. From the satellite’s X/Y position by using the most recent plate solving results the equatorial coordinates are stored in a file together with the current Julian date.

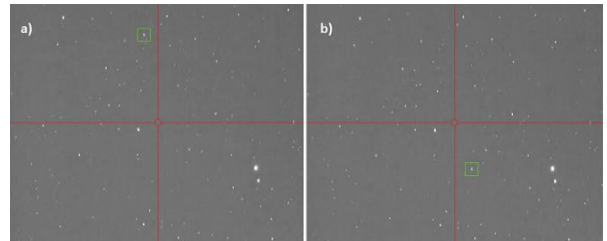


Figure 5-1. Haiyang 2A passes through the camera’s field of view and is automatically detected and highlighted with a green rectangle. Its equatorial coordinates are calculated using a plate solving algorithm.

## 6 SPACE DEBRIS LASER RANGING

### 6.1 Experimental procedure

For the following experiments a 20 Watt / 100 Hz space debris laser with 3 ns pulse width was used which Graz SLR station has on loan from DLR Stuttgart [28]. All targets were first tracked using standard TLE CPFs to collect SLR data which can be later on used for CPF, time and range bias comparison. After successfully ranging with TLE-CPFs the telescope was moved along track corresponding to a time bias of approx. 30 s until the target moved out of the field of view of the stare camera. Then the tracking was stopped and the telescope pointed into this fixed direction of the sky. After a few seconds the target reappeared and passed through the field of view of the camera. The pointing to the satellite was acquired by our software and the data

stored to a file which was then immediately used to generate a new “*Stare and Chase*” CPF with the above mentioned algorithm. The CPF was hence just based on the pointing information and did not use any a-priori orbit information. The whole process from the satellite appearing in the field of view of the *Stare* camera until the reestablishment of tracking with the new CPFs can be completed in less than 2 minutes. After the reestablishment of tracking the target was centered in the field of view of the *stare* camera by adjusting the time or range bias and the standard SLR searching routine was started.

## 6.2 Experimental results

Within a two-day campaign 5 different targets were successfully ranged with the *Stare and Chase* method: three uncooperative “space debris” targets and two LEO satellites. In the following, results are presented for SL-14 R/B (NORAD 33505), GlobalStar M001 (NORAD 25162) and Iridium 61 (NORAD 25263).

The Observed-Minus-Calculated (O-C) residuals [km] of the above mentioned targets (Fig. 6-1) are ranging from approx. 150 m (SL-14 R/B) to 1000 m (GlobalStar M001). For comparison: TLE CPFs ranging had residuals between 30m (SL-14 R/B) and 400 m (Iridium 61).

The CPF offsets of the X/Y/Z Earth-centred earth fixed coordinates of the *Stare & Chase* CPFs are compared to TLE CPFs for the case of SL-14 R/B (Fig. 6-2). On the x-axis the time [min] passed after the first appearance in the field of view is shown. For the first ten minutes the offset is less than 10 km but it increases rapidly to up to 40 km afterwards. This highlights the dependence of the method on rapid establishment of tracking after pointing determination. The faster the tracking can be established the better the CPFs and hence the higher the probability to have success with ranging. The offsets oscillate with a period close to 96 min which corresponds well the orbital period of 95.4 min of SL-14 R/B. After integer values of the orbital period the offsets reach a minimum value, which indicates that there is a small chance of tracking the target at the next revolution. GlobalStar M001 and Iridium 61 showed similar results, though the matching of the oscillation period to the orbital period was not as good as for SL-14 R/B.

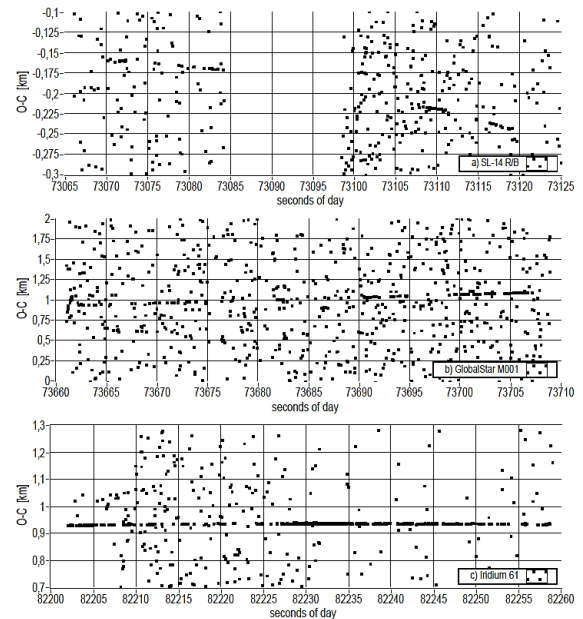


Figure 6-1. Observed-Minus-Calculated Residuals (O-C) in km for SL-14 R/B, GlobalStar M001 and Iridium 61 track by using the CPFs generated only from optically acquired pointing data. The x-axis shows the seconds of day 2016/06/29.

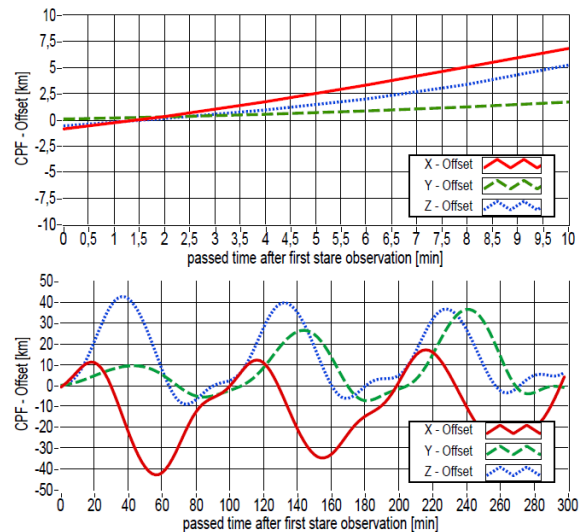


Figure 6-2. CPF offset [km] X/Y/Z Earth-centered earth fixed: *Stare & Chase* CPF – TLE CPF. The results of SL-14 R/B are shown. On the x-axis the passed time after the first appearance in the field of view is shown. For the first ten minutes the offset is less than 10 km but increases rapidly afterwards. The offsets oscillate with a period close to 96 min which corresponds well to its orbital period of 95.4 min.

Comparing the time and range biases of TLE and *Stare and Chase* laser ranging with each other led to similar results. The *Stare and Chase* based tracking had biases

being approx. an order of magnitude larger than tracking with TLE (Tab. 6-1).

Table 6-1. Time biases  $t_b$  and range biases  $r_b$  of SL-14 R/B, GlobalStar M001 and Iridium 61 tracked with TLE CPFs and with Stare and Chase CPFs.

Satellite	TLE		Stare & Chase	
	$t_b$ [ms]	$r_b$ [m]	$t_b$ [ms]	$r_b$ [m]
SL-14 R/B	-23	144	-54	-700
G-Star M001	71	-33	336	1750
Iridium 61	-73	2	108	-764

Monitoring the full duration of the pass of SL-14 R/B it can be seen that the whole process including TLE-based ranging (red), optical pointing determination (blue) and Stare & Chase – based laser ranging (green) can be easily completed within the few minutes of a LEO pass (Fig. 6-3).

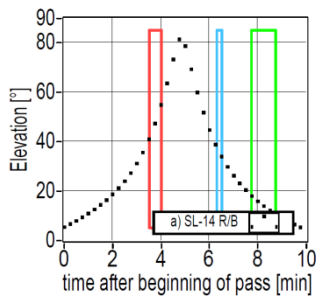


Figure 6-3. Elevation [°] of SL-14 R/B in dependence of the time [min] after the beginning of the pass over Graz SLR station. The three observation phases are: TLE-laser ranging (red), optical pointing determination (blue) and Stare and Chase laser ranging (green). All phases can be easily completed with 10 minutes.

## 7 SUMMARY & CONCLUSION

A full analysis on the orbit determination algorithms for the stare and chase concept was performed. The algorithms were regarding their limits depending on the geometry of the pass and the quality of the observations for various scenarios. An experimental proof of concept was successfully carried out using a LEO telescope and a satellite laser ranging with a high-power space debris laser. Several uncooperative targets were tracked without using a priori orbit information just by compiling the previously acquired pointing angles.

The work of this project was conducted within the ESA project 4000112734/14/D/SR 'Space debris stare and chase'.

## 8 REFERENCES

- Englert, C. R. *et al.* (2014). Optical orbital debris spotter. *Acta Astronaut.* **104**, 99–105.
- Krisko, P. H., Flegel, S., Matney, M. J., Jarkey, D.

- R. & Braun (2015). V. ORDEM 3.0 and MASTER-2009 modeled debris population comparison. *Acta Astronaut.* **113**, 204–211.
- Anz-Meador, P. & Shoots, D. (2016). NASA. *Orbital Debris Q. News* **20**, 1–14.
- Voersmann, P. & Wiedemann, C. (2012). Space Debris - Current Situation. 1–12. Online at <http://www.unoosa.org/pdf/pres/lsc2012/tech-02E.pdf>
- Kessler, D. J. & Cour-Palais, B. G. (1978). Collision frequency of artificial satellites: The creation of a debris belt. *J. Geophys. Res.* **83**, 2637–2646.
- Steindorfer, M. A., Kirchner, G., Koidl, F. & Wang, P. (2015). Light Curve Measurements with Single Photon Counters at Graz SLR. *2015 ILRS Technical Workshop* 1–7.
- Kirchner, G., Hausleitner, W. & Cristea, E. (2007). Ajisai spin parameter determination using Graz kilohertz satellite laser ranging data. *IEEE T. Geosci. Remote* **45**, 201–205.
- Otsubo, T. (2000). Spin motion of the AJISAI satellite derived from spectral analysis of laser ranging data. *IEEE T. Geosci. Remote* **38**, 1417–1424.
- Kucharski, D. *et al.* (2014). Attitude and spin period of space debris envisat measured by satellite laser ranging. *IEEE T. Geosci. Remote* **52**, 7651–7657.
- Michal, T., Eglizeaud, J.-P. & Bouchard, J. (2005). GRAVES: The new French System for Space Surveillance. in *Proceedings of the Fourth European Conference of Space Debris*.
- Mehrholz, D., Leushacke, L. & Banka, D. (2004). Beam-park experiments at FGAN. **34**, 863–871.
- Jehnl, R. (2001). Comparison of the 1999 Beam-park experiment results with space debris models. **28**, 1367–1375.
- Wirnsberger, H., Baur, O. & Kirchner, G. (2015). Space Debris Orbit Predictions using Bi - Static Laser Observations . Case Study : ENVISAT. *Adv. Sp. Res.* **55**, 1–17.
- Degnan, J. J. (1993). Millimeter Accuracy Satellite Laser Ranging: A Review. *Contrib. Sp. Geod. to Geodyn. Technol.* **25**, 133–162.
- Kirchner, G. *et al.* (2013). Laser measurements to space debris from Graz SLR station. *Adv. Sp. Res.* **51**, 21–24.
- Kirchner, G. *et al.* (2013). Multistatic Laser Ranging to Space Debris. *18th Int. Work. Laser*

*Ranging* 1–6.

17. Fujimoto, K., Maruskin, J. M. & Scheeres, D. J. (2010). Circular and zero-inclination solutions for optical observations of Earth-orbiting objects - Fujimoto.pdf.
18. Beutler, G. (2005). *Methods of celestial mechanics Vol I, Physical, Mathematical and Numerical Principles*.
19. Vallado, D. A. & McClain, W. D. (1997). *Fundamentals of Astrodynamics and Applications*, McGraw-Hill.
20. Gooding, R. H. (1993). A new Procedure of Orbit Determination.
21. Vallado, D. A. (2004). Evaluating Gooding Angles-only Orbit Determination of Space Based Space Surveillance Measurements with existing ground based sensors for several reasons 1–22.
22. Izzo, D. Revisiting Lambert's problem. (2014). doi:10.1007/s10569-014-9587-y
23. Watec Cameras Inc. Watec 910HX/RC. Online at <http://www.wateccameras.com/>
24. Tagawa, M., Yanagisawa, T., Kurosaki, H., Oda, H. & Hanada, T. (2016). Orbital objects detection algorithm using faint streaks. *Adv. Sp. Res.* **57**, 929–937.
25. Gruntman, M. (2014) Passive optical detection of submillimeter and millimeter size space debris in low Earth orbit. *Acta Astronaut.* **105**, 156–170.
26. Hampf, D., Wagner, P. & Riede, W. (2015). Optical technologies for the observation of low Earth orbit objects. *65th International Astronautical Congress* 1–8
27. DC-3 Dreams. PinPoint Astrometric Engine. Online at <http://pinpoint.dc3.com/>
28. Deutsches Zentrum für Luft- und Raumfahrt e. V. (DLR). Online at <http://www.dlr.de/>